ACS APPLIED MATERIALS & INTERFACES

www.acsami.org

Research Article

Calligraphy of Nanoplasmonic Bioink-Based Multiplex Immunosensor for Precision Immune Monitoring and Modulation

Jiacheng He, Siqi Wu, Wu Chen, Albert Kim, Wen Yang, Chuanyu Wang, Zhengyang Gu, Jialiang Shen, Siyuan Dai, Weiqiang Chen, and Pengyu Chen*

Cite This: *ACS Appl. Mater. Interfaces* 2023, 15, 50047−50057

Read Online

ACCESS | Metrics & More | Article Recommendations | Supporting Information

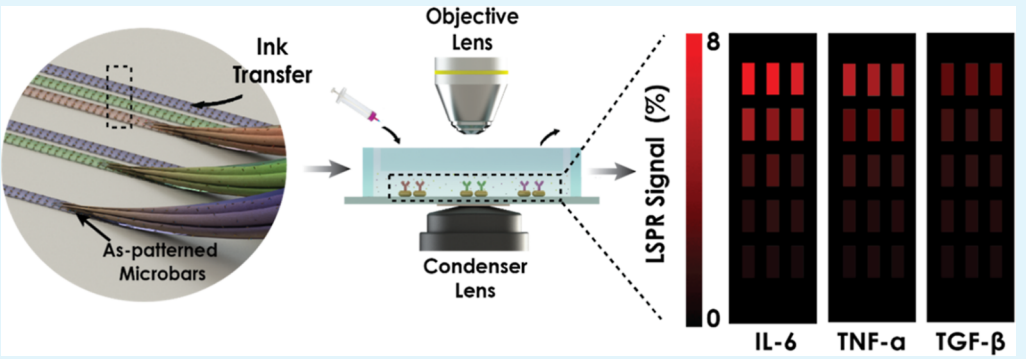

ABSTRACT: Immunomodulation therapies have attracted immense interest recently for the treatment of immune-related diseases, such as cancer and viral infections. This new wave of enthusiasm for immunomodulators, predominantly revolving around cytokines, has spurred emerging needs and opportunities for novel immune monitoring and diagnostic tools. Considering the highly dynamic immune status and limited window for therapeutic intervention, precise real-time detection of cytokines is critical to effectively monitor and manage the immune system and optimize the therapeutic outcome. The clinical success of such a rapid, sensitive, multiplex immunoanalytical platform further requires the system to have ease of integration and fabrication for sample sparing and large-scale production toward massive parallel analysis. In this article, we developed a nanoplasmonic bioink-based, label-free, multiplex immunosensor that can be readily "written" onto a glass substrate via one-step calligraphy patterning. This facile nanolithography technique allows programmable patterning of a minimum of 3 μL of nanoplasmonic bioink in 1 min and thus enables fabrication of a nanoplasmonic microarray immunosensor with 2 h simple incubation. The developed immunosensor was successfully applied for real-time, parallel detection of multiple cytokines (e.g., interleukin-6 (IL-6), tumor necrosis factor-alpha (TNF-α), and transforming growth factor-beta (TGF-β)) in immunomodulated macrophage samples. This integrated platform synergistically incorporates the concepts of nanosynthesis, nanofabrication, and nanobiosensing, showing great potential in the scalable production of label-free multiplex immunosensing devices with superior analytical performance for clinical applications in immunodiagnostics and immunotherapy.

KEYWORDS: *nanolithography, localized surface plasmon resonance (LSPR), microfluidics, multiplexed immunosensors, cytokines, immunomodulation*

INTRODUCTION

Immunotherapy has long been used as a promising way to treat allergies, reduce transplant rejection, and dampen autoimmunity against acute inflammatory diseases.[1−3] The latest immunomodulation approach, targeting a specific set of immune pathways, has been adapted as a new generation of immunotherapies to battle cancer, autoimmune diseases, and viral infections.[4] The ongoing global health crisis due to COVID-19 further places immunotherapies at the forefront, where anticytokine storm treatment has been regarded as one of the most effective and safe methods for treating patients with the virus. Yet, the limited time window for therapeutic intervention, as well as the simultaneous occurrence of pro-inflammatory and anti-inflammatory responses in acute phases, pose significant practical challenges in immunomodulation. Emerging biosensing technologies are critically needed for rapid and accurate immune diagnosis to tightly monitor and regulate the immune system for better therapeutic management and clinical outcomes.

Received: August 2, 2023
Accepted: September 26, 2023
Published: October 19, 2023

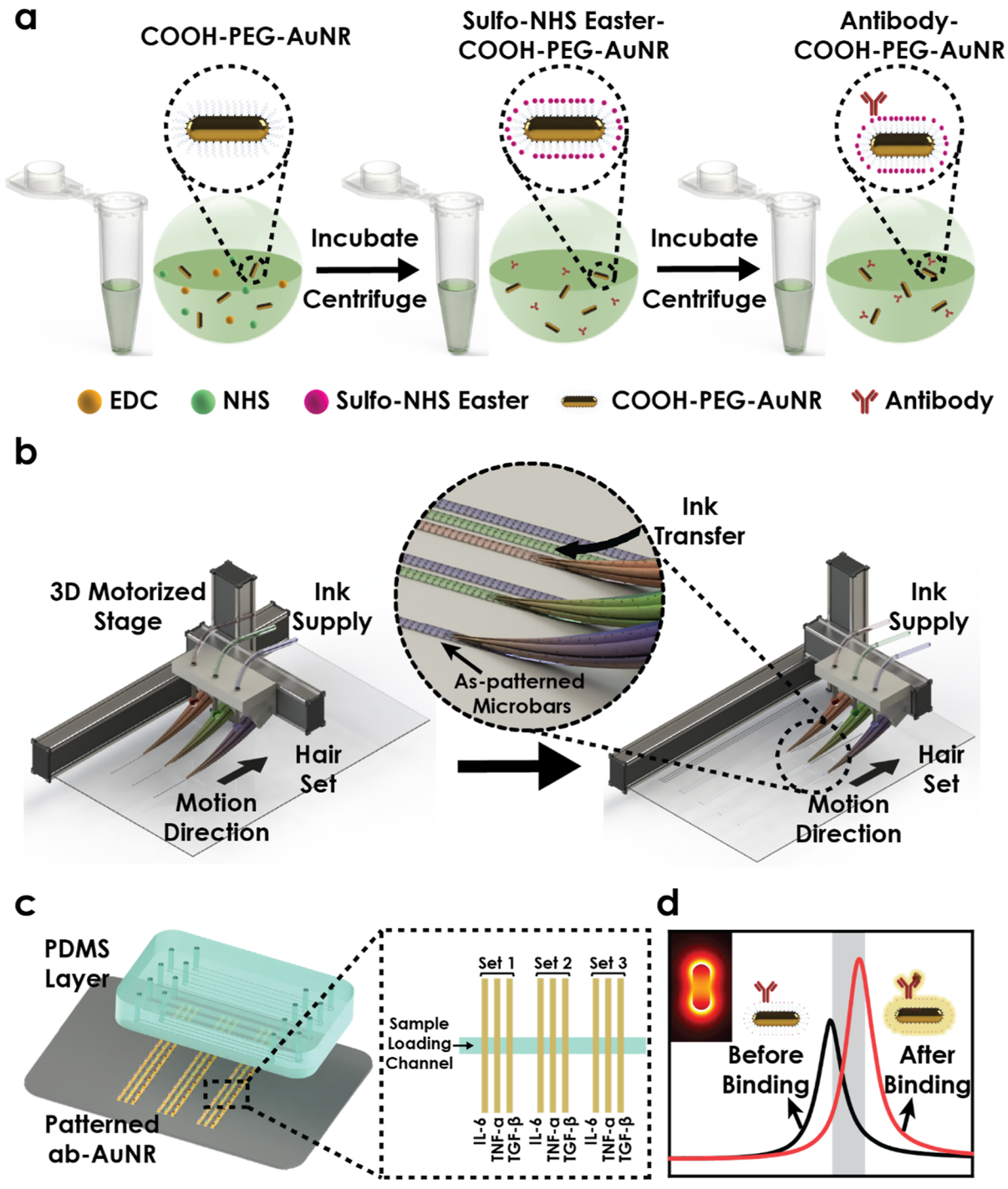

Figure 1. (a) Schematic of solution-based synthesis strategy of antibody conjugated gold nanorods. EDC and NHS are first added for PEG-COOH-AuNR surface activation. Then, corresponding antibodies are conjugated with activated PEG-COOH-AuNR in phosphate buffer. Betaine is introduced to control the evaporation behavior of the nanoplasmonic bioinks. The steric hindrance effect provided by PEG helps prevent nanoparticle agglomeration. (b) 3D illustration of calligraphy patterning technique. A homemade motorized stage allows for programmable motion along three axes. Three sets of weasel hairs are immobilized on the holder and three types of nanoplasmonic bioinks are supplied through corresponding plastic tubing. During the patterning process, the 3D-stage first descends in the *Z* axis, causing the weasel hairs to touch the substrate. The deformation of weasel hairs disturbs the equilibrium between gravitational force and curvature gradient-aroused Laplace pressure, enabling controlled nanoplasmonic bioink transfer. Inset: the illustration of liquid transfer. Three types of nanoplasmonic bioinks were simultaneously transferred onto the substrate. (c) Left: illustration of a LSPR immunosensor. A piece of PDMS layer with microfluidic channels on the bottom was placed on the as-fabricated LSPR chip. Right: magnified view of the patterned LSPR chip. Each chip is patterned with three sets of nanoplasmonic bioink, each set containing three types of bioink. Thus, each sample loading results in triplicate measurements for statistical analysis. (d) Electromagnetic field simulations reveal that the binding events between cytokine and antibody resulted in a red-shifted spectrum and higher scattering intensity. Inset: electromagnetic field distribution of a gold nanorod.

https://doi.org/10.1021/acsami.3c11417
ACS Appl. Mater. Interfaces 2023, 15, 50047−50057

Cytokines are critical mediators in regulating the immune system via the cytokine network and play essential roles in the modulation of immune responses. Enzyme-linked immunosorbent assay (ELISA) has been a widely accepted practice for cytokine quantification. However, the complex labeling and washing processes limit its capability for real-time measuring of the elevation or downregulation of cytokine signaling cascades in response to infection or therapeutic interventions.[5] Recent efforts in nanobiosensing have enabled new formats of immunoassays, where localized surface plasmon resonance (LSPR) nanobiosensors have shown great advantages in monitoring cytokine profile alterations.[6,7] By harnessing the unique optical responses of noble metal nanoparticles (NPs) at the local nanosurface, label-free cytokine detection with high spatiotemporal resolution can be achieved.[8] The assembly of bioconjugated NPs into multiplex arrays offers a transformative approach to examine panels of physiologically relevant cytokines in a time- and cost-effective manner.[9] A variety of advanced nanofabrication techniques have thus been applied for the development of nanomaterial-based multiarray immunosensors, inclusive of microfluidic patterning, microcontact printing, e-beam lithography, dip-pen nanolithography, and inkjet printing.[5,10−14] Microfluidics and microcontact printing rely on predesigned mask layers to generate desired NP patterns, while other mask-free techniques typically need sophisticated instrumentation under stringent processing conditions (i.e., high energy radiation and high vacuum).[15] Subsequent immobilization and bioconjugation are further required to biofunctionalize the fabricated NP pattern for multiplex immunoassays, which complicate device fabrication and impede scalable production of the immunosensing devices toward potential clinical usage.[16]

Recent studies on hierarchically anisotropic microstructures of weasel hairs have shown effective transportation of pristine NP suspensions onto various types of substrates.[17,18] Inspired by such a mask-free direct patterning approach, we developed a novel easy-to-implement patterning strategy with outstanding printability to fabricate a new type of label-free, multiplex microfluidic LSPR cytokine immunosensor (Figure 1). In this strategy, anticytokine-antibody-conjugated gold nanorod (AuNR-Ab conjugate) suspensions are served as "ready-to-use" nanoplasmonic bioinks, and a facile yet effective "one-step" calligraphy method is used to directly "write" the nanoplasmonic bioinks on a glass substrate to generate multiplex immunosensing arrays as the immunosensor. This patterning strategy (i) only requires a 1 min programmed mechanical operation followed by a 2 h simple incubation with a minimum of 3 μL of nanoplasmonic bioink; (ii) shows excellent flexibility in finely tuning the width and particle density of the patterned AuNR-Ab conjugate stripes through adjusting experimental parameters, including weasel hair number, tilt angle, and deformed distance; and (iii) allows fabrication of highly multiplex immunosensors that can be customized to accommodate a wide array of target species based on specific requirements. The fabricated LSPR immunosensors were employed to detect interleukin-6 (IL-6), tumor necrosis factor-alpha (TNF-α), and transforming growth factor-β (TGF-β) expressions in macrophage-associated immunomodulation, demonstrating their capacity for rapid, sensitive, selective, and high-throughput detection of multiple cytokines toward precision immune monitoring and modulation in complex biological matrices.

RESULTS AND DISCUSSION

Design, Fabrication, and Principle of the Label-Free, Multiplex LSPR Cytokine Immunosensor. Figure 1 illustrates the construction processes (Figure 1a−c) and sensing principle (Figure 1c,d) of the label-free, multiplex LSPR immunosensor fabricated through one-step calligraphy patterning of nanoplasmonic bioinks on a glass substrate. Based on the strategy, the immunosensor can be adapted to detect a wide range of cytokines, customizable to the specific requirements of a given application. Here the immunosensor is configured for simultaneous detection of three different types of cytokines, including IL-6, TNF-α, and TGF-β. These particular cytokines were selected due to their significant roles in immune responses and during the process of immunomodulation.

The nanoplasmonic bioinks developed here are the aqueous suspensions of AuNR-Ab conjugates dispersed in 5 mM phosphate-buffered saline (PBS, pH 7.4) with the addition of 9 M betaine (Figure 1a). It is important to note that betaine was added last into the aqueous suspensions of the prepared AuNR-Ab conjugates. This step was to prevent the evaporation of the water in the suspensions (Figure S1 in Supporting Information), ensuring that the AuNR-Ab conjugate suspensions maintained a consistent particle concentration throughout the storage and the calligraphy patterning process. Three types of nanoplasmonic bioinks were designed in this work, each consisting of aqueous suspensions of different conjugates: AuNR-anti-IL-6, AuNR-anti-TNF-α, and AuNR-anti-TGF-β. The calligraphy patterning system is a customized 3D motorized stage equipped with three key components: (i) three parallel sets of weasel hairs (N = 5) for direct calligraphy utilizing the three different nanoplasmonic bioinks, (ii) a computer with a customized MATLAB code for programmable motion of the weasel hairs along three axes, and (iii) a pair of syringe pumps for controlled injection of the three nanoplasmonic bioinks onto the corresponding sets of weasel hairs (see Figures 1b and S2). By controlled calligraphy patterning, we can fabricate three sets of AuNR-Ab conjugate stripes on a glass surface, each targeting a different cytokine: IL-6, TNF-α, and TGF-β, respectively.

The AuNR-Ab-conjugate-stripe patterned glass is attached to a polydimethylsiloxane (PDMS) sample-flow layer, featuring 8 parallel microfluidic sample channels (each accommodating a 300 nL sample volume). These channels are arranged perpendicular to the three sets of AuNR-Ab conjugate stripes on the glass substrate (Figure 1c). As a result, we create a label-free, multiplex microfluidic LSPR immunosensing chip with 9 sample channels, 3 segments of parallel collocating AuNR-anti-IL-6-Ab, AuNR-anti-TNF-α-Ab, and AuNR-anti-TGF-β-Ab conjugate arrays in each channel, and a total of 72 square immunosensing arrays (200 μm × 200 μm) for the entire chip.

The sensing principle of this multiplex immunosensor aligns with those described in our previous reports regarding label-free LSPR immunosensors.[19] As shown in Figure 1d (COMSOL simulation), when target cytokines (i.e., IL-6, TNF-α, and TGF-β) are introduced into the immunosensor, they are captured by their corresponding anticytokine antibodies on the AuNR-Ab-conjugate arrays. The binding results in a red-shift in the wavelength and an intensity increase of the major LSPR scattering peak of the AuNRs present on the arrays, triggered by the alteration in the local refractive index around the AuNRs.[20] This heightened light-scattering response can be easily measured in real time using a dark-field scattering imaging technique developed previously by our research group.[21]

https://doi.org/10.1021/acsami.3c11417
ACS Appl. Mater. Interfaces 2023, 15, 50047−50057

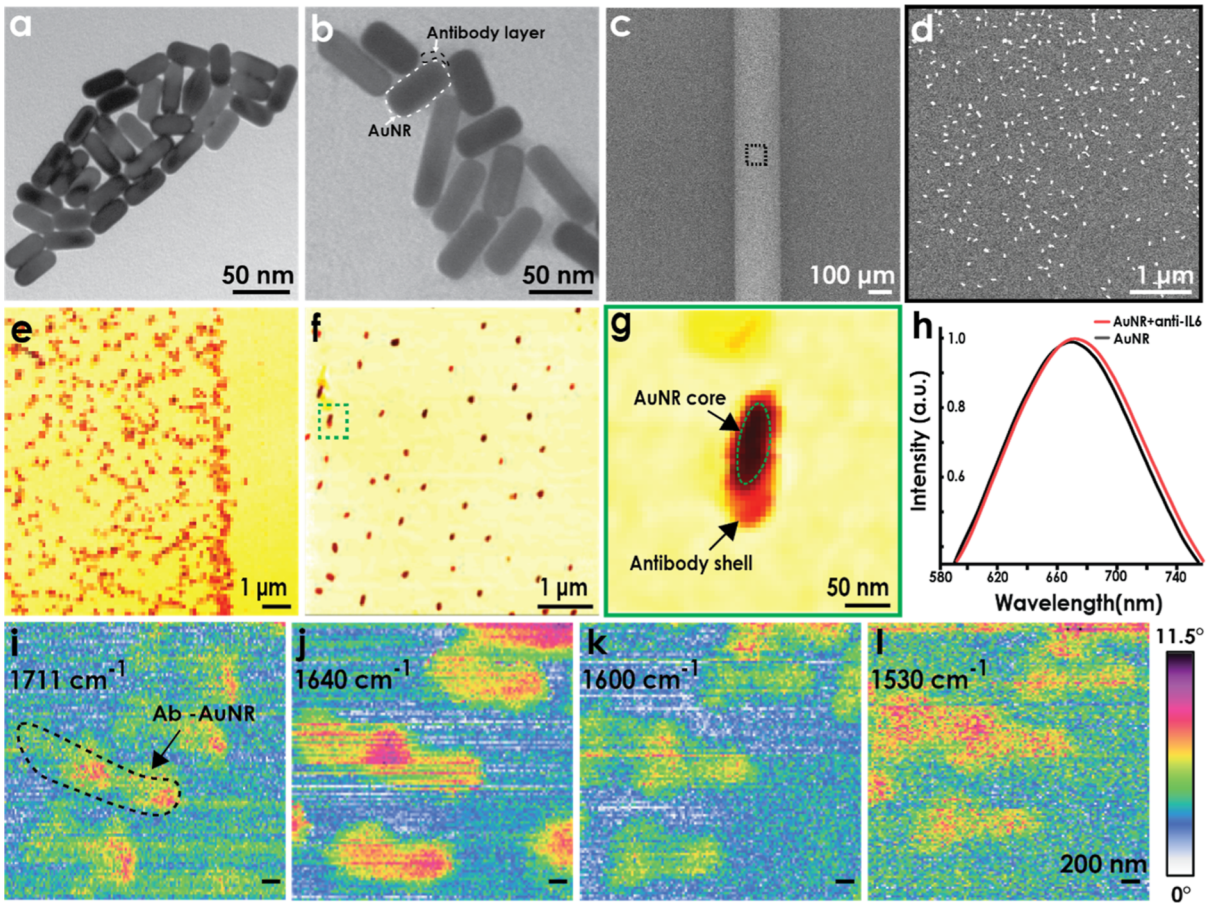

Figure 2. TEM images of AuNR-PEG-COOH (a) and antibody conjugated AuNRs (b). SEM image showing the width of the patterned stripe (c) and the surface distribution of the antibody conjugated AuNRs (d). s-SNOM amplitude image of patterned anti-IL-6-PEG-COOH-AuNRs (e,f). Zoom-in s-SNOM amplitude image of a single anti-IL-6-PEG-COOH-AuNR (g). The UV−vis spectra of PEG-COOH-AuNRs and anti-IL-6-PEG-COOH-AuNRs (h). The s-SNOM phase images of patterned antibody conjugated AuNRs at various frequencies (i−l).

Table 1. Wavelength, Hydrodynamic Size, and Zeta Potential of AuNRs and Three Types of Antibodies Conjugated AuNRs

parameters	AuNR	anti-IL-6-AuNR	anti-IL-6-AuNR with betaine	anti-TNF-α-AuNR	anti-TNF-α-AuNR with betaine	anti-TGF-β-AuNR	anti-TGF-β-AuNR with betaine
λ (nm)	661.67 ± 0.02	663.26 ± 0.02	663.47 ± 0.02	664.45 ± 0.01	663.62 ± 0.02	663.38 ± 0.02	663.61 ± 0.05
size (nm)	37.82 ± 0.37	42.18 ± 0.76	42.56 ± 0.20	43.38 ± 0.48	44.96 ± 0.09	40.93 ± 0.76	43.58 ± 0.20
zeta potential (mv)	−32.23 ± 0.74	−31.93 ± 1.10	−36.37 ± 0.99	−27.60 ± 1.31	−29.1 ± 0.95	−34.37 ± 2.02	−37.00 ± 1.47

Consequently, the concentration of target cytokines can be accurately determined by the measured light-scattering response signals.

Preparation and Characterization of AuNR-Ab Conjugates as Nanoplasmonic Bioinks. The nanoplasmonic bioinks (i.e., AuNR-Ab conjugate aqueous suspensions) were synthesized by conjugating polyethylene-glycol-carboxyl- (PEG-COOH−) capped AuNRs[19,22] of 41 nm length and 17 nm diameter (Figure 2a). The formation of AuNR-Ab conjugates was verified by transmission electron microscopy (TEM) (Figure 2b), UV−vis extinction spectroscopy (Figure 2h), dynamic light scattering (DLS), and zeta potential measurements (summarized in Table 1). As indicated by the UV−vis spectra in Figure 2h, the longitudinal LSPR extinction peak of the AuNR-PEG-COOHs underwent a red-shift from 661 to 663 nm after modification with anticytokine antibodies, suggesting the presence of antibodies on the surface of AuNR-PEG-COOHs due to a higher refractive index of antibody than water.[23] The constructed antibody-nanoparticle conjugate barcode was characterized by using scanning electron microscopy (SEM) (Figure 2c−d). As shown in Figure 2c, the width of the patterned barcode was measured to be ∼132 μm. Figure 2d presents homogeneously distributed anti-IL-6 conjugated AuNRs within the enlarged central area of the pattern.

The quality and distribution of patterned antibody-conjugated AuNRs were further investigated by scattering-type scanning near-field optical microscopy (s-SNOM) (Figure 2e−g), showing results consistent with those of the SEM images. The s-SNOM image (Figure 2g) shows isolated anti-IL-6-PEG-COOH-AuNRs on the barcode, with the dark core representing the PEG-COOH-AuNR, covered by the coated shell, indicative of antibody conjugation. Upon irradiation with incident infrared (IR) at varying frequencies, the antibody layer was further confirmed by analyzing the scattering amplitude of the s-SNOM images at 1530, 1600, 1640, and 1711 cm^{-1} (Figure 2i−l). Here,

https://doi.org/10.1021/acsami.3c11417
ACS Appl. Mater. Interfaces 2023, 15, 50047−50057

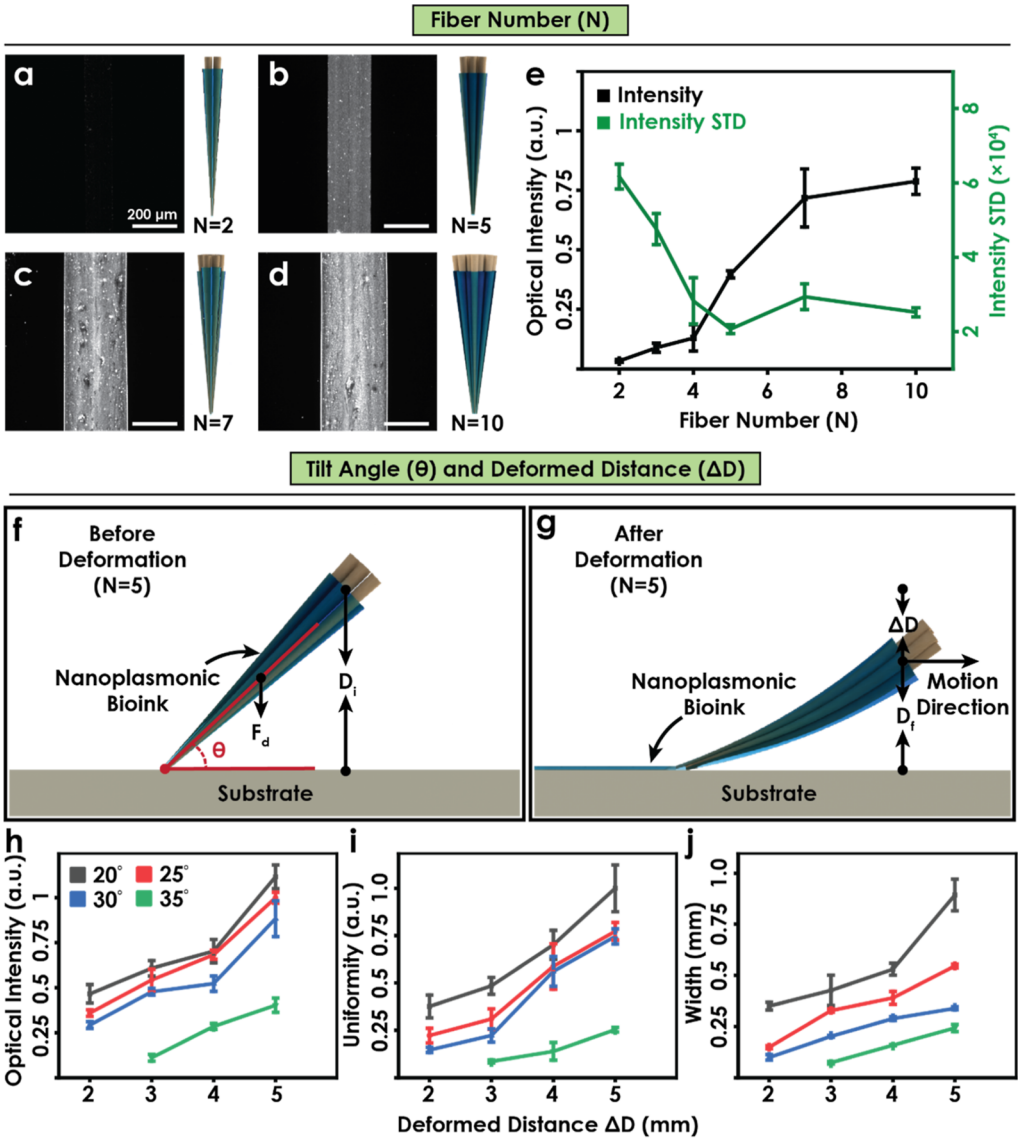

Figure 3. Flexibility in controlling the plasmonic nanoparticle density, microbar uniformity, and width achieved by tuning weasel hair number (N), tilt angle (θ), and deformed distance (ΔD). (a–d) Left: dark-field images of microbars patterned by varying the number of weasel hair (N). The images of three and four weasel hair system are not shown here. Right: illustration of differing numbers of weasel hair employed during patterning process. (a) Two weasel hair system; (b) five weasel hair system; (c) seven weasel hair system; (d) ten weasel hair system. Dark-field images were analyzed, and results are summarized in (e). The plasmonic nanoparticle density (black) was indicated by average scattering intensity on the microarray. The uniformity was evaluated by the standard deviation of scattering intensity on each pixel (olive). (f,g) Schematics of nanoplasmonic bioink trapped among weasel hairs ($N = 5$) before and after hair deformation. The tilt angle (θ) was defined by the angle between substrate surface and weasel hairs without deformation. Deformed distance (ΔD) was given by the difference between initial distance (D_i) and final distance (D_f). Nanoparticle density (h), uniformity (i), and width (j) can be finely tuned by controlling tilt angle and deformed distance.

the chosen frequencies, specifically 1530 and 1640 cm^{-1}, correspond to the absorption peaks associated with the β-sheet structure (amide band II) and the α-helix structure (amide band I), respectively. The inclusion of 1600 cm^{-1} (dip between the amide band I and amide band II) and 1711 cm^{-1} (out of the amide band range) serves as the comparative controls in the measurements. Our data revealed the strongest and the weakest amplitude at 1640 and 1600 cm^{-1}, respectively, in agreement with previous observations.[24] These results collectively demonstrate the successful formation of highly monodispersed, negatively charged AuNR-Ab conjugates, enabling the production of three nanoplasmonic bioinks (i.e., aqueous suspensions of AuNR-anti-IL-6-Ab, AuNR-anti-TNF-α-Ab, and AuNR-anti-TGF-β-Ab conjugates) for the subsequent construction of the multiplex immunosensor.

One-Step Calligraphy Patterning of Nanoplasmonic Bioinks. In a standard calligraphy patterning process, the three nanoplasmonic bioinks were continuously supplied onto three sets of weasel hairs with syringe pumps and then guided to "write" three different nanoplasmonic bioink stripes on the amino-silanized glass surface using the MATLAB code-controlled 3D motorized stage. After incubation, the negatively charged AuNR-Ab bioink can firmly adhere to the positively charged amino-silanized glass surface, resulting in three separate AuNR-Ab conjugate stripes on the glass surface. (See Figures 1b and S2 and Methods for details).

https://doi.org/10.1021/acsami.3c11417
ACS Appl. Mater. Interfaces 2023, 15, 50047−50057

Figure 3a−d presents typical dark-field scattering images of the AuNR-Ab conjugate stripes with varying fiber numbers generated from a standard calligraphy patterning. It can be observed that the AuNR-Ab conjugate stripes displayed strong light-scattering signals owing to the LSPR scattering property of AuNRs when the fiber number is 5 or above. The scattering signals were uniformly distributed across the entire stripes, suggesting that the AuNR-Ab conjugate stripes can be patterned with a highly uniform particle distribution. The widths of all 9 stripes were measured to be around 191 μm, with narrow distributions (3.6 μm in standard deviations) based on the analysis of 10 different areas for each stripe. Meanwhile, the overall average stripe width was calculated to be 192 $\pm$ 2.5 μm, with a low coefficient of variation of 1.3%, indicating that the AuNR-Ab conjugate stripes can be readily prepared with high width uniformity. These results demonstrate the successful patterning of high-quality AuNR-Ab conjugate stripes on glass substrates via the developed calligraphy patterning of nanoplasmonic bioinks. The procedures of this calligraphy patterning method are notably straightforward, only requiring 1 min of programmed mechanical operation and a 2 h incubation to pattern three sets of different AuNR-Ab conjugate stripes on a glass substrate. This approach achieves one-step fabrication of a multiplex immunosensing chip in approximately 2 h, offering significant advantages for scalable device manufacture. Moreover, the volume of each nanoplasmonic bioink required for patterning of each strip was as low as 3 μL, which greatly reduced the consumption of costly regents (e.g., AuNRs and anticytokine antibodies). In contrast, conventional microfluidic patterning followed by biomodification could take up to ∼12 times as long (∼24 h) to produce the same immunosensing chip, with much more complicated multistep procedures and larger consumption of expensive regents.

It should be highlighted that our one-step calligraphy patterning method exhibits high flexibility in tuning the nanoparticle density (characterized by the scattering intensity of the patterned microbars) and width of the nanoplasmonic bioink stripes. This can be achieved by adeptly controlling four key parameters: AuNR-Ab particle concentration ($C_{\text{AuNR-Ab conjugates}}$), weasel hair number ($N$), tilt angle ($\theta$), and deformed distance (ΔD). The precise control over the nanoparticle density and width of encoding AuNR-Ab sensing stripes plays a critical role as it determines the sensing sensitivity and multiplexing capacity of label-free LSPR immunosensors. As illustrated in Figures 3a−d and S3, the nanoplasmonic bioink stripes can be patterned by altering the weasel hair number, with the corresponding effects on the nanoparticle density and intensity standard deviation plotted in Figure 3e. With fewer weasel hairs (fibers) involved, the optical intensity of the stripe tends to decrease with larger signal variation due to a reduced volume of the plasmonic ink supplied by the fewer hairs. This could result in diminished sensitivity and a reduced dynamic range owing to the lack of sufficient binding sites. In a scenario where nanoparticle density is excessively high, when using a high number of weasel hairs, we encounter plasmonic coupling that leads to a broadened scattering peak in our real-time measurements. Notably, when using five weasel hairs, we achieved the most controllable process, as indicated by the minimized standard deviation of the scattering light intensity.

By fixing the weasel hair number at 5, we further demonstrated that both the nanoparticle density and width of the nanoplasmonic bioink stripes can be finely adjusted within the ranges of 0.15−1 au/μm^2 and 100−1000 μm, respectively. Such precise tuning was achieved by altering the tilt angle between 20 and 35° and the deformed distance in the range of 2−5 mm (Figure 3f−j). As shown in Figure 3h, higher scattering intensities of the patterned strips were observed at smaller tilt angles in general, especially under configurations of small angles with extensive deformed distances. Similar trends can be observed for microbar uniformity and width (Figure 3i,j). Such trends can be explained by the loss of Laplace pressure, which arises from the larger curvature gradient near the weasel hair tip. When the weasel hairs were deformed during the patterning process, the upward Laplace force was perturbed. As a result, the nanoplasmonic bioink can be transferred onto the substrate mainly due to the unopposed gravitational force. As the deformation distance increases, the effective Laplace pressure decreases, leading to an enhanced transfer of gold nanorods. However, it is important to note that while enhanced nanoparticle density, uniformity, and width can be achieved by increasing the deformed distance at a smaller tilt angle, excessive bioink transfers coupled with unpredictable evaporation dynamics would result in scattered bright spots and a coffee-ring effect[25] that compromise the pattern quality and sensing performance.

The results above have demonstrated the ability of the calligraphy method to give highly sophisticated patterning control. Moreover, we can perform separate parameter adjustments on the optical density of the microbars by altering the concentration of NPs in the bioink prior to the patterning. Meanwhile, by adjusting the parameters, including tilt angle and deformed distance, during the pattern process, the breadth of the stripes can be controlled correspondingly. In contrast, conventional microfluidic patterning combined with biomodification methods falls short in the flexibility of patterning control, especially on the nanoparticle density and width of sensing stripes, which would require a tedious and costly process involving the design and fabrication of numerous molds for PDMS microfluidic mask layers with varying widths of microfluidic channels. The simplicity and speed of our one-step calligraphy patterning approach, combined with the low volume requirements for nanoplasmonic bioinks, could facilitate high-throughput, cost-effective production of immunosensors, paving the way for advanced, high-throughput immune monitoring and immunomodulatory investigations.

To optimize the quality of LSPR light-scattering imaging using our dark-field microscope (under a 10× objective lens), we set the weasel hair number, tilt angle, and deformed distance at N = 5, θ = 35°, and ΔD = 5 mm, respectively. The resulting width of the nanoplasmonic bioink stripes was found to be around 192 μm. Under these conditions, we further investigated the effect of the AuNR-Ab particle concentration used for patterning the nanoplasmonic bioink stripes on the sensing performance.

Detection of Cytokines Using the Fabricated LSPR Immunosensor. To assess the utility of the fabricated label-free multiplex microfluidic LSPR immunosensor for cytokine detection, we evaluated its response to a mixture of cytokine standards containing IL-6, TNF-α, and TGF-β. The cytokine mixture was introduced into the microfluidic sample channels of the immunosensing chip (Figure 1c), with each of the 8 channels that can afford triplicate measurements of the cytokines.

Under optimal conditions, we evaluated the sensor's performance metrics, including sensitivity, dynamic range, precision, specificity, accuracy, and reliability. The assessment was conducted according to the following standard detection

https://doi.org/10.1021/acsami.3c11417
ACS Appl. Mater. Interfaces 2023, 15, 50047−50057

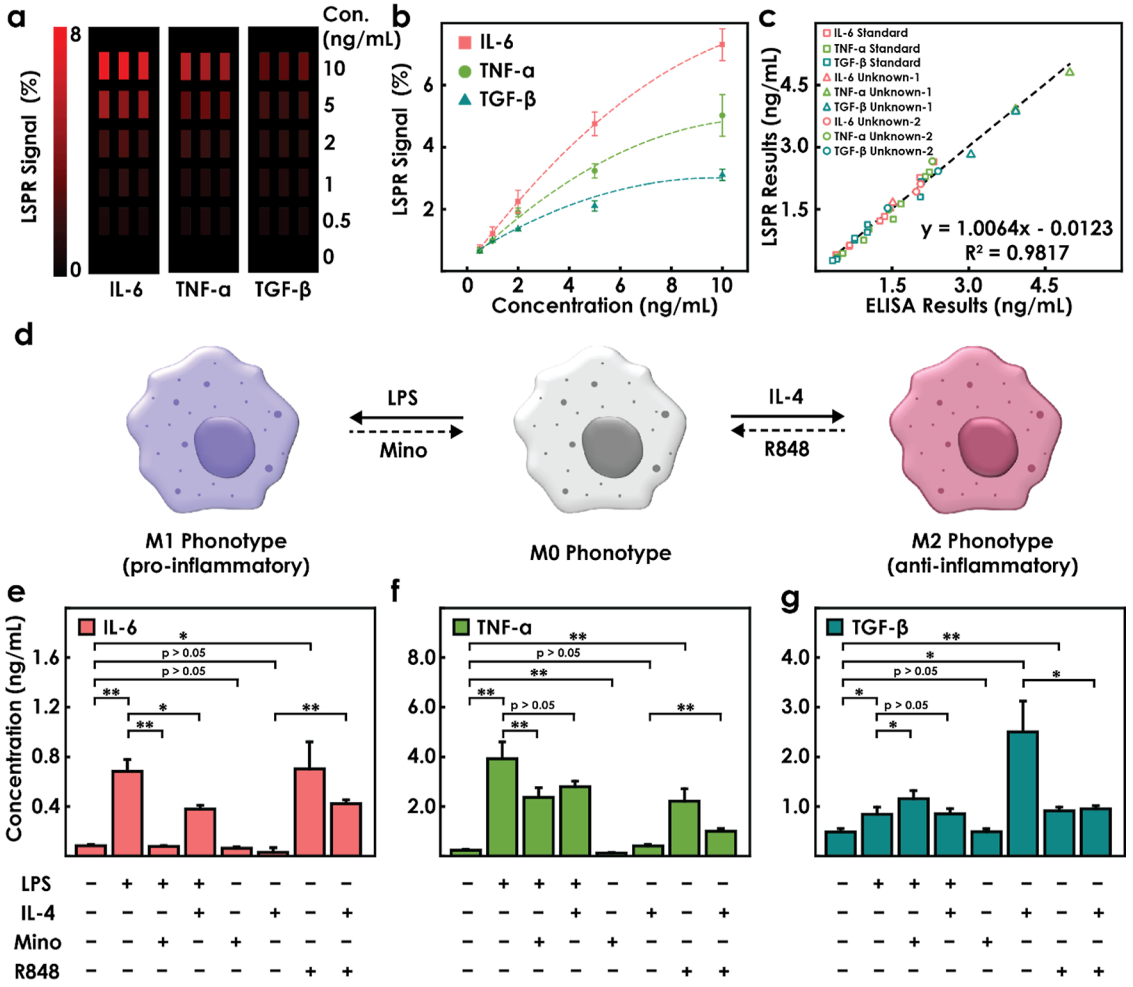

Figure 4. (a) Concentration-dependent scattering intensity heat map based on LSPR signal change. Known concentrations of IL-6, TNF-α, and TGF-β were spiked in cell culture medium and injected into microfluidic channel. The images were taken every 10 s for 30 min. (b) Calibration curves of IL-6, TNF-α, and TGF-β calculated from LSPR microbar intensity mapping in (a). The limits of detection for IL-6, TNF- α, and TGF-β were 40.93, 69.15, and 93.67 pg/mL, respectively. (c) Correlation between LSPR and ELISA results. Three samples with known concentration of IL-6, TNF-α, and TGF-β and two macrophage samples with unknown concentration were measured by both methods. (d) Schematics of macrophage polarization and immunomodulation treatments. Primary macrophages (M0) were treated by LPS, IL-4, minocycline and R848 and incubated for 24 h. The macrophage culture mediums in different treatment groups were collected for LSPR measurements. (e–g) IL-6, TNF-α, and TGF-β secretion profiles of macrophage samples under different treatment conditions.

procedures: (i) the immunosensing chip was mounted on the microscope and exposed to multicytokine standards (or samples) of varying concentrations, followed by a 30 min incubation at room temperature and a subsequent washing step and (ii) during the incubation, the scattering light intensity of every immunosensing microarray was captured in real-time using the microscope. The variation ratio ($\Delta I/I_0$) of the scattering light intensity of each microarray, both before (I_0) and after ($I_0 + \Delta I$) the sample loading, was calculated as the signal for detection (see Methods and Figure S4 for details).

The sensitivity and dynamic range of the immunosensor were first evaluated by analyzing its response to multicytokine standards containing IL-6, TNF-α, and TGF-β at different concentrations of 500, 1000, 2000, 5000, and 10,000 pg/mL. Figure 4a depicts the concentration-dependent heat map results (calculated based on the intensity variations in real dark-field images using MATLAB) of the intensity variation ratio ($\Delta I/I_0$) for the detection of multicytokine standards with concentrations ranging from 0 to 10,000 pg mL $^{-1}$. For each type of cytokine, $\Delta I/I_0$, serving as the detection signal, increased proportionally with the cytokine concentration. Calibration curves of the immunosensor for the three target cytokines were obtained by plotting the $\Delta I/I_0$ values against the target cytokine concentration (Figure 4b). For all three cytokines, the $\Delta I/I_0$ could be clearly differentiated in the concentration range of 1–10,000 pg mL^{-1} (spanning 4 orders of magnitude), suggesting a relatively wide response range of the immunosensor for multiplex cytokine detection. The binding specificity of the immunosensor was probed by incubating with an interferon-γ (IFN-γ) sample solution, showing negligible signal change for the patterned immunosensor (Figure S5). The limits of detection (LODs) of the immunosensor were calculated to be 40.93 pg mL^{-1} for IL-6, 69.15 pg mL^{-1} for TNF-α, and 93.67 pg mL^{-1} for TGF-β based on the 3-sigma method, where LOD is equal to the target concentration corresponding to a signal that is 3 times the standard deviation (SD) above the zero baseline. These findings demonstrate that our immunosensor could be applied for sensitive multiplex detection of cytokines with a wide dynamic range. It should be noted that such efficient detection only requires a total assay time of 40 min, including sample loading,

https://doi.org/10.1021/acsami.3c11417
ACS Appl. Mater. Interfaces 2023, 15, 50047–50057

incubation, washing, image acquisition, processing and analysis, and result output.

To demonstrate the potential application of the developed immunosensor for real sample detection, it was utilized to analyze two macrophage samples and three cytokine-spiked samples. The detection results were cross-verified with the existing gold-standard method, i.e., ELISA. All 5 samples were analyzed following the standard assay procedure, and the cytokines in each sample were quantified based on the calibration curves shown in Figure 4b. The obtained quantification data were compared to reference results quantified by commercially available cytokine ELISA kits. The comparison was carried out based on the linear regression analysis between the detection results obtained by the two methods. As indicated in Figure 4c, a robust positive correlation was found between the cytokine concentrations measured by our immunosensor and those reported by the reference ELISA, with a correlation coefficient of $R^2 = 0.98$, a slope of 1.006, and an intercept of −0.01, all very close to their corresponding ideal values. These results demonstrate the high accuracy and reliability of our immunosensor in analyzing low-level cytokines in complex real samples, suggesting its great potential for practical application.

Considering the above evaluation results of the immunosensor's performance, it is worth mentioning that the overall sensing performance of our multiplex label-free LSPR immunosensor is comparable to those of previously reported multiplex label-free LSPR immunosensors. However, our immunosensor features a rapid, simple, and efficient fabrication process based on the calligraphy patterning method, in contrast to the complicated and time-consuming conventional microfluidic patterning fabrication employed by previous immunosensors. This implies that the simplicity and efficiency of our calligraphy patterning method do not compromise the sensing performance of multiplex label-free LSPR immunosensors, showing significant advantages of our immunosensor in scalable production toward clinical applications.

Application in Profiling Cytokine Expression in Immune Monitoring and Immunomodulation. Finally, we applied the developed immunosensor to explore cytokine expression characteristics in immunomodulation in macrophage differentiation. Macrophages are multifunctional cells with heterogeneous subpopulations derived from bone marrow and yolk sac progenitors. They play an indispensable role in triggering, guiding, and terminating the adaptive immune response through the release of cytokines.[26,27] Macrophages exhibit phenotypic polarization into two extreme subtypes, namely classically (M1) and alternatively (M2) activated macrophages.[28] The M1 phenotype macrophages promote inflammation and inhibit tumor progression by secreting high levels of pro-inflammatory cytokines, such as IL-6 and TNF-α. While M2 phenotype macrophages inhibit inflammation and promote the proliferation of tumors through the release of anti-inflammatory cytokines such as TGF-β.[6,29]

To monitor the IL-6, TNF-α, and TGF-β expression profiles in various immunomodulated macrophage differentiation processes, we conducted several control experiments as illustrated in Figure 4d: (i) the original macrophages (M0, sample 1) were polarized into M1 (sample 2) and M2 (sample 6) phenotype macrophages using lipopolysaccharides (LPS) and interleukin-4 (IL-4), respectively; (ii) minocycline (Mino) and resiquimod (R848) were then introduced as the immunomodulators to the M1 and M2 phenotype macrophage samples to inhibit the hyperinflammatory response of M1 phenotype macrophages (sample 3)[30] and to promote the inflammatory response M2 phenotype macrophages (sample 8),[31] (iii) LPS + IL-4, minocycline, and R848 were also incubated with M0 macrophages as the control samples (sample 4, 5, and 7), respectively, and (iv) the IL-6, TNF-α, and TGF-β levels in these 8 immunomodulated macrophage samples were simultaneously quantified using our developed immunosensor. Within only 40 min, we completed three replicate quantifications of the three target cytokines in the 8 macrophage samples by carrying out a total of 72 tests on a single immunosensing chip, reaffirming the simplicity, speediness, multiplex, and high throughput capabilities of our immunosensor in performing such massively parallel tests. As evidenced from the cytokine profiles obtained from the 8 immunomodulated macrophage samples (Figure 4e−g), the M0 macrophages did not exhibit significant secretion of any of the three target cytokines. When M0 macrophages were polarized into M1 phenotype macrophages with the stimulation of LPS, they expressed high levels of pro-inflammatory cytokines (IL-6 and TNF-α) and low levels of anti-inflammatory cytokine (TGF-β). When M1 phenotype macrophages were further stimulated by minocycline, pro-inflammatory cytokine expression was significantly suppressed, while anti-inflammatory cytokine expression was boosted. Conversely, M2 phenotype macrophages polarized from M0 macrophages by IL-4 showed a significantly increased secretion of anti-inflammatory cytokine (TGF-β) and greatly suppressed proinflammatory responses, as indicated by the low IL-6 and TNF-α secretions. Further R848 treatment of M2 phenotype macrophages resulted in an upregulation of pro-inflammatory cytokines and suppression of anti-inflammatory cytokines. For the control group treated with both LPS and IL-4, an increase in all three cytokines was observed, indicating that both M1 and M2 phenotypes were expressed. The measured results were also validated by ELISA, producing similar trends to those observed with our immunosensor, as illustrated in Figure S6. These data demonstrate that our immunosensor showed excellent sensing capability for cytokine expression profiles in immunomodulation in a biomimetic stimulation environment, which could have far-reaching applications, especially in point-of-care inflammation-related disease diagnosis and routine immune status monitoring.

CONCLUSIONS

In this study, we demonstrated a label-free, multiplex LSPR microfluidic immunosensor that can simultaneously analyze multiple cytokines in a rapid, sensitive, specific, accurate, and high-throughput manner. The novelty of our approach lies in the integration of "ready-to-use" nanoplasmonic bioinks composed of AuNR-Ab conjugates with a unique, self-developed calligraphy patterning system. This facile yet efficient one-step calligraphy patterning technique possesses exceptional print flexibility. It allows direct inscription of the nanoplasmonic bioinks on a glass substrate to generate high-quality multiplex immunosensing arrays, thereby reducing the fabrication of the immunosensor to a brief 1 min programmed mechanical operation and a simple 2 h incubation. Such a streamlined fabrication process contrasts favorably with many previously reported nanofabrication patterning techniques that often require complicated and time-consuming steps. The fabricated immunosensor was demonstrated to allow simultaneous detection of three cytokines in triplicates of 8 different samples (6 μL each) per immunochip, with a low detection limit down to

https://doi.org/10.1021/acsami.3c11417
ACS Appl. Mater. Interfaces 2023, 15, 50047−50057

40 pg mL^{-1} level, a wide linear dynamic range of 4 orders of magnitude, and a short assay time under 40 min. Using the commercial gold-standard ELISA as a benchmark method, the immunosensor was validated for practical use in the measurement of cytokines in real samples with excellent accuracy and reliability. The potential application of the immunosensor was verified through the analysis of cytokine expression profiles in macrophage-related immunomodulation, rendering it a robust tool for point-of-care immune diagnosis and monitoring. Due to the inherent flexibility of the one-step calligraphy patterning technique, the scope of the immunosensor could be easily expanded for the detection of additional cytokines, thereby enabling more comprehensive functional analysis of the immune system. The concept of controllable calligraphy patterning using bioinks could be extrapolated to the fabrication of many other types of biosensing chips, paving the way for the design and creation of novel microfluidic biosensors that can be utilized across a variety of basic and applied research.

METHODS

Preparation of Anti-Cytokine Antibody Conjugated Gold Nanorods (AuNR-Ab Conjugates) as the Nanoplasmonic Bioinks. The three types of AuNR-Ab conjugates were prepared by modifying AuNR-PEG-COOHs (with a diameter of ~17 nm and a length of ~41 nm) with three types of anticytokine antibodies, including anti-IL-6, anti-TNF-α, and anti-TGF-β antibodies, using an EDC/NHS coupling method.[32,33] Briefly, 10 μL of a 17 × 41 nm AuNR-PEG-COOH aqueous suspension (1.6 mg/mL, nanoComposix, Inc.) was incubated with 3 μL of a 20 mM EDC and 35 mM NHS aqueous solution at room temperature for 30 min, followed by centrifugation at 6000 rpm for 9 min. The supernatant was discarded, and the obtained precipitates (i.e., EDC/NHS-activated AuNR-PEG-COOHs) were washed twice with deionized (DI) water and then resuspended in 10 μL of 0.5% PEG in PBS buffer (pH 7.4). Subsequently, 1 μL of a 50 μg mL^{-1} anticytokine antibody solution was added to the EDC/NHS-activated AuNR-PEG-COOH suspension. After 1 h of incubation at room temperature, 10 μL of 10% BSA in PBS buffer (pH 7.4) was added to the mixture and incubated for an additional 1 h at room temperature. After centrifugation and washing again, the products (i.e., AuNR-Ab conjugates) were suspended in 30 μL of PBS buffer (pH 7.4) containing 9 M betaine, 1% BSA, 0.05% Tween 20, and 0.02% NaN_3. The final AuNR-Ab conjugate suspension was stored at 4 °C for future use.

Preparation of Amino-Silanized Glass. The amino-silanized glass was prepared by functionalizing a glass slide with (3-aminopropyl) triethoxysilane (APTES) through a concentrated vapor-phase deposition technique.[34] Briefly, a glass slide was soaked in Piranha solution (H_2SO_4 (98%)/H_2O_2 (30%) = 3/1, v/v) for 15 min. After rinsing with DI water, the cleaned glass slide was ultrasonicated in DI water for 15 min and then dried in an oven at 65 °C for 15 min. Following the cleaning process, the glass slide was placed on the mouth of a Petri dish in a desiccator, and 0.5 mL of APTES liquid was added into the Petri dish. The desiccator was vacuumed for 2 h, followed by 2-day incubation under the vacuum at room temperature. To further fix the APTES molecules on the glass surface, the APTES-functionalized glass layer was placed in an oven at 100 °C for 30 min, resulting in the generation of a negatively charged amino-terminated silane monolayer on the glass surface. Finally, the prepared amino-silanized glass was stored at room temperature for future use.

Fabrication of Microfluidic Sample-Flow Polydimethylsiloxane Mask Layer. The sample-flow polydimethylsiloxane (PDMS) mask layer was designed to contain 8 sets of parallel straight microfluidic channels (dimensions of 3.0 cm (L) × 200 μm (W) × 50 μm (H)) used for loading of detection samples. This PDMS mask layer was fabricated using soft lithography based on our previously reported procedures.[13,15,22] Initially, a mold for this PDMS mask layer was manufactured on the surface of a silicon substrate via deep reactive ion etching (Deep Silicon Etcher, Surface Technology Systems, Allenton, PA). Subsequently, a PDMS prepolymer was prepared by mixing a silicone elastomer base agent with a curing agent at a mass ratio of 10:1. The resulting PDMS prepolymer was transferred onto the surface of a silicon mold, placed in a vacuum desiccator at room temperature for 30 min, and then cured in an oven at 80 °C for 4 h, leading to the formation of the designed PDMS mask layer. After being peeled off from the silicon mold, the PDMS mask layer was cut into the desired shape, punched to form channel inlets and outlets, and finally stored at room temperature for future use.

Fabrication of the LSPR Immunosensing Chip Using One-Step Calligraphy Patterning Technique. In a standard fabrication, three sets of three different AuNR-Ab conjugate stripes targeting IL-6, TNF-α, and TGF-β were first generated on a glass surface through one-step calligraphy patterning of three different types of nanoplasmonic bioinks (AuNR-anti-IL-6, AuNR-anti-TNF-α, and AuNR-anti-TGF-β aqueous suspensions) on an amino-silanized glass surface. Specifically, the three different types of nanoplasmonic bioinks were continuously injected onto the surfaces of three sets of weasel hairs (N = 5), respectively, at a rate of 1 μL/min using syringe pumps. The nanoplasmonic bioinks were retained among the weasel hairs due to a balance between gravitational force and curvature gradient-aroused Laplace pressure.[18] The weasel hairs containing the nanoplasmonic bioinks were then controlled to make contact with the amino-silanized glass surface at a tilt angle of 20° and a deformed distance of 5 mm. They were guided to draw three sets of three nanoplasmonic bioink stripes on the amino-silanized glass surface by the MATLAB code-driven 3D motorized stage. During this process, the aforementioned balance was perturbed, facilitating the controllable transfer of the nanoplasmonic bioinks onto the glass surface. After 2 h of incubation, the negatively charged AuNR-Ab conjugates in the nanoplasmonic bioinks were firmly immobilized on the positively charged amino-silanized glass surface owing to the electrostatic interactions between the AuNR-Ab conjugates and the glass surface, forming the three sets of three different AuNR-Ab conjugate stripes on the glass surface. The microfluidic sample-flow PDMS mask layer prepared above was attached onto the as-formed AuNR-Ab-conjugate-stripe-patterned glass. The microfluidic sample channels of the PDMS mask layer were arranged perpendicular to the AuNR-Ab conjugate stripes and were physically attached to the LSPR chip followed by gently pressing by hand. The microfluidic sample channels were loaded with cell culture medium for blocking the nonspecific binding sites in the channels. Finally, the fabricated multi-AuNR-Ab-conjugate-arrayed microfluidic chip was stored at 4 °C for future use.

Detection of Multiple Cytokines Using the Fabricated LSPR Immunosensor. Prior to detection, multicytokine standards of varying concentrations, ranging from 0 to 10,000

https://doi.org/10.1021/acsami.3c11417
ACS Appl. Mater. Interfaces 2023, 15, 50047−50057

pg mL^{-1} were prepared by dissolving IL-6, TNF-α, and TGF-β together in cell culture medium. An upright dark-field optical microscope was used for measurements throughout the detection (see Supporting Information for detailed microscope configuration). In a standard detection procedure, the fabricated multi-AuNR-Ab-conjugate-microarrayed LSPR immunosensing chip was mounted on the motorized $X-Y$ stage of the dark-field optical microscope for positioning of the sensing area. The PDMS sample loading layer was not removed during the process to allow real-time signal monitoring during the incubation. The oil immersion dark-field condenser was then attached to the back of the LSPR immunosensing chip, thus allowing the incident light to illuminate the chip. Subsequently, each of the microfluidic sample channels of the chip was loaded with multicytokine standards or samples at a flow rate of 1 μL/min with a syringe pump. After incubation at room temperature for 30 min, each of the channels was washed with PBS buffer (pH 7.4) containing 0.05% Tween 20 (PBST) at a flow rate of 0.2 μL/min for 5 min. During this period, automated image scanning was performed on the immunosensing microarrays of the chip at a rate of 72 sensing spots to acquire the dark-field image of each immunosensing microarray. The light scattered from each immunosensing microarray was collected by a 10× objective lens, filtered by a band-pass filter (670 ± 25 nm), imaged by an electron-multiplying charge-coupled device (EMCCD) camera, and eventually recorded by the NIS-Element BR analysis software. Finally, the variation ratio ($\Delta I/I_0$) of the scattering light intensity for each immunosensing microarray, before (I_0) and after ($I_0 + \Delta I$) sample loading, was calculated as the detection signal. This data analysis was automatically processed by our customized Matlab program.

■ ASSOCIATED CONTENT

Supporting Information

The Supporting Information is available free of charge at https://pubs.acs.org/doi/10.1021/acsami.3c11417.

Detailed experimental description; effect of betaine on evaporation; calligraphy patterning system configuration; dark-field images of the patterned stripes under different conditions; and dark-field system setup (PDF)

■ AUTHOR INFORMATION

Corresponding Author

Pengyu Chen − *Materials Research and Education Center, Auburn University, Auburn, Alabama 36849, United States;* orcid.org/0000-0003-3380-872X; Email: pengyuc@auburn.edu

Authors

Jiacheng He − *Materials Research and Education Center, Auburn University, Auburn, Alabama 36849, United States;* orcid.org/0000-0002-1940-4262

Siqi Wu − *Materials Research and Education Center, Auburn University, Auburn, Alabama 36849, United States*

Wu Chen − *Department of Drug Discovery and Development, Harrison School of Pharmacy, Auburn University, Auburn, Alabama 36849, United States*

Albert Kim − *Materials Research and Education Center, Auburn University, Auburn, Alabama 36849, United States; Center for Medicine, Health, and Society, Vanderbilt University, Nashville, Tennessee 37235, United States*

Wen Yang − *Materials Research and Education Center, Auburn University, Auburn, Alabama 36849, United States*

Chuanyu Wang − *Materials Research and Education Center, Auburn University, Auburn, Alabama 36849, United States*

Zhengyang Gu − *Materials Research and Education Center, Auburn University, Auburn, Alabama 36849, United States*

Jialiang Shen − *Materials Research and Education Center, Auburn University, Auburn, Alabama 36849, United States*

Siyuan Dai − *Materials Research and Education Center, Auburn University, Auburn, Alabama 36849, United States;* orcid.org/0000-0001-7259-7182

Weiqiang Chen − *Department of Mechanical and Aerospace Engineering, New York University, New York, New York 11201, United States; Department of Biomedical Engineering, New York University, Brooklyn, New York 11201, United States;* orcid.org/0000-0002-9469-8328

Complete contact information is available at: https://pubs.acs.org/10.1021/acsami.3c11417

Author Contributions

P.C. and J.H. conceived the project. Z.G. and J.H. designed the 3D stage. J.H., S.W., and A.K. performed UV−vis spectrometry, dynamic light scattering, and zeta potential measurement. W.Y., C.W., J.S., and S.D. performed SEM, TEM, AFM, and s-SNOM characterizations. J.H. and A.K. patterned and conducted immunoassay. J.H. and W.C. performed cell culture and ELISA validation. J.H. performed electromagnetic field simulation. J.H. conducted data analysis and designed the schematics. P.C., S.W., W.C., and J.H. wrote the paper. All authors discussed the data and agreed on the manuscript.

Notes

The authors declare no competing financial interest.

■ ACKNOWLEDGMENTS

This work was supported by the National Institutes of Health (NIH) MIRA R35GM133795 and National Science Foundation (NSF) CAREER CBET-1943302 (P.C.), NIH MIRA R35GM133646 and NSF CBET 2103219 (W. Chen), NSF OIA-2033454 and ACS PRF Fund 66229-DNI6 (S.D.), and the Alabama Graduate Research Scholars Program (GRSP) by the Alabama EPSCoR (J.S.).

■ REFERENCES

(1) Andersson, R.; Andersson, B.; Andersson, E.; Eckerwall, G.; Norden, M.; Tingstedt, B. Immunomodulation in Surgical Practice. *HPB* **2006**, *8* (2), 116−123.

(2) Liang, H.; Jin, C.; Ma, L.; Feng, X. B.; Deng, X. Y.; Wu, S. L.; Liu, X. M.; Yang, C. Accelerated Bone Regeneration by Gold-Nanoparticle-Loaded Mesoporous Silica through Stimulating Immunomodulation. *ACS Appl. Mater. Interfaces* **2019**, *11* (44), 41758−41769.

(3) Knopf-Marques, H.; Singh, S.; Htwe, S. S.; Wolfova, L.; Buffa, R.; Bacharouche, J.; Francius, G.; Voegel, J. C.; Schaaf, P.; Ghaemmaghami, A. M.; Vrana, N. E.; Lavalle, P. Immunomodulation with Self-Crosslinked Polyelectrolyte Multilayer-Based Coatings. *Biomacromolecules* **2016**, *17* (6), 2189−2198.

(4) Iqbal Yatoo, M.; Hamid, Z.; Rather, I.; Nazir, Q. U.; Bhat, R. A.; Ul Haq, A.; Magray, S. N.; Haq, Z.; Sah, R.; Tiwari, R.; Natesan, S.; Bilal, M.; Harapan, H.; Dhama, K. Immunotherapies and Immunomodulatory Approaches in Clinical Trials-A Mini Review. *Hum. Vacc. Immunother.* **2021**, *17* (7), 1897−1909.

(5) Chen, P.; Huang, N. T.; Chung, M. T.; Cornell, T. T.; Kurabayashi, K. Label-Free Cytokine Micro- and Nano-Biosensing towards Personalized Medicine of Systemic Inflammatory Disorders. *Adv. Drug Deliv. Rev.* **2015**, *95*, 90−103.

(6) Zhu, J.; He, J.; Verano, M.; Brimmo, A. T.; Glia, A.; Qasaimeh, M. A.; Chen, P.; Aleman, J. O.; Chen, W. An Integrated Adipose-Tissue-on-Chip Nanoplasmonic Biosensing Platform for Investigating Obesity-Associated Inflammation. *Lab Chip* **2018**, *18* (23), 3550−3560.
(7) Javed, I.; He, J.; Kakinen, A.; Faridi, A.; Yang, W.; Davis, T. P.; Ke, P. C.; Chen, P. Probing the Aggregation and Immune Response of Human Islet Amyloid Polypeptides with Ligand-Stabilized Gold Nanoparticles. *ACS Appl. Mater. Interfaces* **2019**, *11* (11), 10462−10471.
(8) Malekzad, H.; Sahandi Zangabad, P.; Mirshekari, H.; Karimi, M.; Hamblin, M. R. Noble Metal Nanoparticles in Biosensors: Recent Studies and Applications. *Nanotechnol. Rev.* **2017**, *6* (3), 301−329.
(9) He, J.; Brimmo, A. T.; Qasaimeh, M. A.; Chen, P.; Chen, W. Recent Advances and Perspectives in Microfluidics-Based Single-Cell Biosensing Techniques. *Small Methods* **2017**, *1* (10), 1700192.
(10) Hou, J.; Liu, T.; Chen, R.; Liu, J.; Chen, J.; Zhao, C.; Yin, L.; Li, C.; Xu, X.; Shi, Q.; Yin, J. Guided Protein/Cell Patterning on Superhydrophilic Polymer Brushes Functionalized with Mussel-Inspired Polydopamine Coatings. *Chem. Commun.* **2017**, *53* (50), 6708−6711.
(11) Corletto, A.; Yu, L. P.; Shearer, C. J.; Gibson, C. T.; Shapter, J. G. Direct-Patterning SWCNTs Using Dip Pen Nanolithography for SWCNT/Silicon Solar Cells. *Small* **2018**, *14* (16), No. e1800247.
(12) Zhang, Z. L.; Zhang, X. Y.; Xin, Z. Q.; Deng, M. M.; Wen, Y. Q.; Song, Y. L. Controlled Inkjetting of a Conductive Pattern of Silver Nanoparticles Based on the Coffee-Ring Effect. *Adv. Mater.* **2013**, *25* (46), 6714−6718.
(13) Wevers, N. R.; Kasi, D. G.; Gray, T.; Wilschut, K. J.; Smith, B.; van Vught, R.; Shimizu, F.; Sano, Y.; Kanda, T.; Marsh, G.; Trietsch, S. J.; Vulto, P.; Lanz, H. L.; Obermeier, B. A Perfused Human Blood-Brain Barrier on-a-Chip for High-Throughput Assessment of Barrier Function and Antibody Transport. *Fluids Barriers CNS* **2018**, *15*, 23.
(14) Kim, C.; Lee, H.; Devaraj, V.; Kim, W. G.; Lee, Y.; Kim, Y.; Jeong, N. N.; Choi, E. J.; Baek, S. H.; Han, D. W.; Sun, H.; Oh, J. W. Hierarchical Cluster Analysis of Medical Chemicals Detected by a Bacteriophage-Based Colorimetric Sensor Array. *Nanomaterials* **2020**, *10* (1), 121.
(15) Lau, U. Y.; Saxer, S. S.; Lee, J.; Bat, E.; Maynard, H. D. Direct Write Protein Patterns for Multiplexed Cytokine Detection from Live Cells Using Electron Beam Lithography. *ACS Nano* **2016**, *10* (1), 723−729.
(16) Oliverio, M.; Perotto, S.; Messina, G. C.; Lovato, L.; De Angelis, F. Chemical Functionalization of Plasmonic Surface Biosensors: A Tutorial Review on Issues, Strategies, and Costs. *ACS Appl. Mater. Interfaces* **2017**, *9* (35), 29394−29411.
(17) Wang, Q.; Meng, Q.; Wang, P.; Liu, H.; Jiang, L. Bio-Inspired Direct Patterning Functional Nanothin Microlines: Controllable Liquid Transfer. *ACS Nano* **2015**, *9* (4), 4362−4370.
(18) Wang, Q.; Su, B.; Liu, H.; Jiang, L. Chinese Brushes: Controllable Liquid Transfer in Ratchet Conical Hairs. *Adv. Mater.* **2014**, *26* (28), 4889−4894.
(19) Chen, P.; Chung, M. T.; McHugh, W.; Nidetz, R.; Li, Y.; Fu, J.; Cornell, T. T.; Shanley, T. P.; Kurabayashi, K. Multiplex Serum Cytokine Immunoassay Using Nanoplasmonic Biosensor Microarrays. *ACS Nano* **2015**, *9* (4), 4173−4181.
(20) Guo, L. H.; Kim, D. H. LSPR Biomolecular Assay with High Sensitivity Induced by Aptamer-Antigen-Antibody Sandwich Complex. *Biosens. Bioelectron.* **2012**, *31* (1), 567−570.
(21) Wang, C.; Huang, C. H.; Gao, Z.; Shen, J.; He, J.; MacLachlan, A.; Ma, C.; Chang, Y.; Yang, W.; Cai, Y.; Lou, Y.; Dai, S.; Chen, W.; Li, F.; Chen, P. Nanoplasmonic Sandwich Immunoassay for Tumor-Derived Exosome Detection and Exosomal PD-L1 Profiling. *ACS Sens.* **2021**, *6* (9), 3308−3319.
(22) Nusz, G. J.; Curry, A. C.; Marinakos, S. M.; Wax, A.; Chilkoti, A. Rational Selection of Gold Nanorod Geometry for Label-Free Plasmonic Biosensors. *ACS Nano* **2009**, *3* (4), 795−806.
(23) Hall, W. P.; Ngatia, S. N.; Van Duyne, R. P. LSPR Biosensor Signal Enhancement Using Nanoparticle-Antibody Conjugates. *J. Phys. Chem. C* **2011**, *115* (5), 1410−1414.
(24) Amenabar, I.; Poly, S.; Nuansing, W.; Hubrich, E. H.; Govyadinov, A. A.; Huth, F.; Krutokhvostov, R.; Zhang, L.; Knez, M.; Heberle, J.; Bittner, A. M.; Hillenbrand, R. Structural Analysis and Mapping of Individual Protein Complexes by Infrared Nanospectroscopy. *Nat. Commun.* **2013**, *4* (1), 2890.
(25) Kim, D.; Jeong, S.; Park, B. K.; Moon, J. Direct writing of silver conductive patterns: Improvement of Film Morphology and Conductance by Controlling Solvent Compositions. *Appl. Phys. Lett.* **2006**, *89* (26), 264101.
(26) Martinez, F. O.; Sica, A.; Mantovani, A.; Locati, M. J. Macrophage activation and polarization. *Front Biosci.* **2008**, *13*, 453−461.
(27) Noy, R.; Pollard, J. W. Tumor-Associated Macrophages: From Mechanisms to Therapy. *Immunity* **2014**, *41* (1), 49−61.
(28) Murray, P. J. Macrophage Polarization. *Annu. Rev. Physiol.* **2017**, *79* (1), 541−566.
(29) Khabipov, A.; Kading, A.; Liedtke, K. R.; Freund, E.; Partecke, L. I.; Bekeschus, S. RAW 264.7 Macrophage Polarization by Pancreatic Cancer Cells - A Model for Studying Tumour-promoting Macrophages. *Anticancer Res.* **2019**, *39* (6), 2871−2882.
(30) Dutta, K.; Mishra, M. K.; Nazmi, A.; Kumawat, K. L.; Basu, A. Minocycline Differentially Modulates Macrophage Mediated Peripheral Immune Response Following Japanese Encephalitis Virus Infection. *Immunobiology* **2010**, *215* (11), 884−893.
(31) Lee, M.; Park, C.-S.; Lee, Y.-R.; Im, S.-A.; Song, S.; Lee, C.-K. Resiquimod, a TLR7/8 Agonist, Promotes Differentiation of Myeloid-Derived Suppressor Cells into Macrophages and Dendritic Cells. *Arch Pharm. Res.* **2014**, *37* (9), 1234−1240.
(32) Gao, Z. Q.; Song, Y. J.; Hsiao, T.; He, J. C.; Wang, C. Y.; Shen, J. L.; MacLachlan, A.; Dai, S. Y.; Singer, B. H.; Kurabayashi, K.; Chen, P. Machine-Learning-Assisted Microfluidic Nanoplasmonic Digital Immunoassay for Cytokine Storm Profiling in COVID-19 Patients. *ACS Nano* **2021**, *15* (11), 18023−18036.
(33) Hermanson, G. T. *Bioconjugate Techniques*, 2nd; Academic Press: Amsterdam, The Netherlands, 2008, pp 219−223.
(34) Wang, W.; Vaughn, M. W. Morphology and Amine Accessibility of (3-Aminopropyl) Triethoxysilane Films on Glass Surfaces. *Scanning* **2008**, *30* (2), 65−77.

https://doi.org/10.1021/acsami.3c11417
ACS Appl. Mater. Interfaces 2023, 15, 50047−50057